

OPEN ACCESS

# The Effect of Proton Conductivity of Fe–N–C–Based Cathode on PEM Fuel cell Performance

To cite this article: Tatyana Reshетенko *et al* 2020 *J. Electrochem. Soc.* **167** 084501

View the [article online](#) for updates and enhancements.



**PRIME<sup>TM</sup>**  
PACIFIC RIM MEETING  
ON ELECTROCHEMICAL  
AND SOLID STATE SCIENCE  
**2020**


*Abstract Submission*  
**DEADLINE EXTENDED:**  
*May 1, 2020*

**Honolulu, HI | October 4-9, 2020**




# The Effect of Proton Conductivity of Fe–N–C–Based Cathode on PEM Fuel cell Performance

Tatyana Reshetenko,<sup>1,\*</sup> Günter Randolf,<sup>2</sup> Madeleine Odgaard,<sup>3</sup> Barr Zulevi,<sup>4,\*</sup>  
Alexey Serov,<sup>4,\*</sup> and Andrei Kulikovskiy<sup>5,6,\*</sup> 

<sup>1</sup>Hawaii Natural Energy Institute, University of Hawaii, Honolulu, Hawaii 96822, United States of America

<sup>2</sup>GRandalytics, Honolulu, Hawaii 96822, United States of America

<sup>3</sup>IRD Fuel Cells, LLC; Albuquerque, New Mexico 87113, United States of America

<sup>4</sup>Pajarito Powder, LLC; Albuquerque, New Mexico 87109, United States of America

<sup>5</sup>Forschungszentrum Jülich GmbH, Institute of Energy and Climate Research, IEK-14: Electrochemical Process Engineering, D-52425 Jülich, Germany

<sup>6</sup>Lomonosov Moscow State University, Research Computing Center, 119991 Moscow, Russia

A model-based impedance spectroscopy is used to determine proton conductivity, oxygen transport parameter, double layer capacitance and oxygen reduction reaction (ORR) Tafel slope in the Fe–N–C cathode catalyst layer (CCL) of a PEM fuel cell. Experimental spectra of two cells differing by the membrane thickness only are processed using a physics-based model for PEMFC impedance. The spectra have been measured in the range of current densities from 25 to 800 mA cm<sup>-2</sup>. The ORR Tafel slope of both the cells shows almost linear growth with the current density. In one of the cells, the CCL proton conductivity  $\sigma_p$  strongly decays at the current density of 100 mA cm<sup>-2</sup>; this decay is accompanied by the step growth of the double layer capacitance. Other minor variations of proton conductivity and double layer capacitance with the cell current occur also in a counterphase; presumed origin of this effect is discussed. The oxygen diffusion coefficient in the cathode exhibits explosive growth with the cell current. We attribute this effect to formation of temperature and pressure gradients in the CCL due to strongly non-uniform distribution of ORR rate in the electrode.

© 2020 The Author(s). Published on behalf of The Electrochemical Society by IOP Publishing Limited. This is an open access article distributed under the terms of the Creative Commons Attribution 4.0 License (CC BY, <http://creativecommons.org/licenses/by/4.0/>), which permits unrestricted reuse of the work in any medium, provided the original work is properly cited. [DOI: 10.1149/1945-7111/ab8825]



Manuscript submitted February 5, 2020; revised manuscript received March 23, 2020. Published April 20, 2020.

Supplementary material for this article is available [online](#)

Unique properties of platinum as a catalyst of electrochemical reactions provided worldwide use of this precious metal in fuel cell studies and technology. However, high Pt cost limits marketing of Pt-based devices and vehicles. Standard porous Pt/C-based catalyst layer requires 0.4 mg<sub>Pt</sub> cm<sup>-2</sup>, which translates to nearly 100 g of precious metal for a 100 kW automotive PEM fuel cell stack. Clearly, a less expensive alternative is highly desirable.

At the moment the most promising alternative to Platinum Group Metals (PGMs) Oxygen Reduction Reaction (ORR) catalysts is a class of electrocatalysts consisting of atomically dispersed transition metals (Fe and Mn) in a matrix of carbon and nitrogen, so called M–N–C materials.<sup>1–3</sup> Such types of PGM-free catalysts are inexpensive and possess reasonable activities under fuel cell operation conditions, reaching up to 30% of PGM catalysts activity.<sup>1,2</sup> It was shown computationally and experimentally that catalytic activity towards ORR can foremost be attributed to transition metal M coordinated with several nitrogen atoms—M–N<sub>x</sub>.<sup>4–6</sup> In order to increase activity of M–N–C electro-catalysts, several synthetic approaches were developed, mainly based on the principle to either increase the density of M–N<sub>x</sub> sites or to improve their accessibility through the proper integration into the triple phase boundary.<sup>7</sup> It should be noticed that significant progress in the development of PGM-free ORR catalysts was achieved not only in academia and National Laboratories, but also in the industrial sector. For example, state-of-the-art Fe–N–C catalysts are commercially available on market from the Pajarito Powder, LLC (Albuquerque, NM, USA). These materials are manufactured by proprietary VariPore™ method with a fine control of surface chemistry, bulk chemical composition, level of graphitization and morphology. Due to availability of these materials at the level of hundreds of grams in a single batch, this study was performed with a commercial material from Pajarito Powder, LLC marketed as PMF-011904.

Electrochemical Impedance Spectroscopy (EIS) is an extremely powerful technique for fuel cell characterization and testing.<sup>8–10</sup> All transport and kinetic processes in a cell are eventually linked to transport and conversion of charges, which makes every process “visible” via impedance spectroscopy. However, understanding impedance spectra requires rather sophisticated modeling. After pioneering work of Springer et al.<sup>11</sup> and Eikerling and Kornyshev,<sup>12</sup> over the past two decades, a clear trend of moving from simple equivalent circuits toward physics-based impedance models has been demonstrated in literature.<sup>13–31</sup> There is growing interest in complementary impedance techniques, such as concentration/pressure impedance spectroscopy<sup>32–35</sup> and distribution of relaxation times (DRT).<sup>36</sup> Generally, any macroscopic transient performance model for a fuel cell can be converted to impedance model by standard procedure of linearization and Fourier-transform. However, complexity of the resulting linear system of equations for perturbation amplitudes may limit the use of this system for processing of experimental data. A balance between model complexity and applicability for spectra fitting has to be found.

Proton conductivity  $\sigma_p$  of the cathode catalyst layer (CCL) is one of the key parameters determining fuel cell performance. Poor  $\sigma_p$  leads to strongly non-uniform distribution of ORR rate over the CCL thickness leading to doubling of the apparent Tafel slope.<sup>12,37</sup> Measuring of  $\sigma_p$  in a working fuel cell is, however, a difficult task. The most reliable values of  $\sigma_p$  in classic Pt-based PEMFCs have been obtained from EIS of cells working in a hydrogen pumping regime with zero oxygen concentration on the cathode side.<sup>38,39</sup> In this way, the dependencies of  $\sigma_p$  on ionomer-to-carbon (IC) ratio, relative humidity (RH) of the air flow, temperature etc. have been obtained.<sup>39</sup>

However, much less is known on  $\sigma_p$  in an operating cell. Under current conditions, water generated in the CCL, temperature effects, formation of foreign cations, the presence of ORR intermediates and carbon oxides could strongly affect  $\sigma_p$ . Generally,  $\sigma_p$  can be easily determined if the high frequency (HF) part of the Nyquist spectrum follows the theoretical straight line of 45° slope.<sup>12,40</sup> Accurate EIS

\*Electrochemical Society Member.

<sup>z</sup>E-mail: A.Kulikovskiy@fz-juelich.de

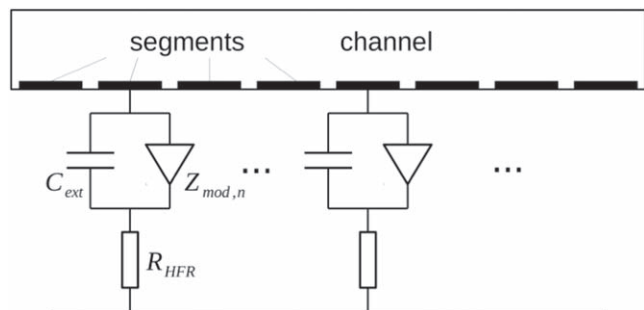


**Figure 1.** Electric circuit representing Eq. 1 for the total cell impedance. For discussion of elements see text.

measurements of  $\sigma_p$  in a Pt-based PEMFC at the cell currents below  $200 \text{ mA cm}^{-2}$  have been done using the spectra having this property in Ref. 41. However, in many cases, the slope of HF part of the spectra greatly exceeds  $45^\circ$ , making determination of  $\sigma_p$  a much more challenging task. To the best of our knowledge, so far  $\sigma_p$  in a working Fe–N–C-based cell has been measured only in Ref. 42. However, HF part of the spectra in Ref. 42 had a slope largely exceeding  $45^\circ$  and to fit this slope, a non-uniform distribution of  $\sigma_p$  through the CCL depth has been assumed (for detailed discussion of this issue see Ref. 43). This assumption led to overestimated values of  $\sigma_p$  in Ref. 42.

Below, we employ a numerical model for PEM fuel cell impedance<sup>44,45</sup> to measure proton and oxygen transport parameters of two PEM fuel cells equipped with the same Fe–N–C-based cathodes and differing by the membrane thickness only. Processing of spectra from two cells gives us more confidence in the resulting parameters (see below). The model is fitted to the spectra measured for the set of current densities from 25 to  $800 \text{ mA cm}^{-2}$ . In this work,  $\sigma_p$  is assumed to be uniform through the CCL depth, and along the electrode active area. The results show strong decay of proton conductivity at the cell current of about  $100 \text{ mA cm}^{-2}$ , unexpected strong correlation between  $\sigma_p$  and the double layer capacitance, significant non-uniformity of the ORR rate over the CCL depth due to relatively low  $\sigma_p$ , and explosive growth of the CCL oxygen diffusivity with the current density. Estimates show that the non-uniformity of the ORR rate through the CCL depth could lead to the temperature and pressure gradients in the CCL. Positive effect of these gradients is CCL “cleaning” from liquid water, making the porous media more transparent for oxygen transport.

### Experimental

The commercial, PGM-free electrocatalyst manufactured by Pajarito Powder and marketed as PMF-011904 was used in the present study. This material was provided to a commercial MEA manufacturer, IRD Fuel Cell, for the integration into the Catalyst Coated Membrane (CCM) electrode by their proprietary digital printing method. Electrochemical evaluation of PGM-free membrane electrode assemblies (MEAs) have been performed using a custom test station, designed at the Hawaii Natural Energy Institute and characterized by dynamic response time  $<0.1 \text{ s}$ . Membrane-electrode assemblies (MEAs) with active area size of  $23 \text{ cm}^2$  were tested at  $80^\circ \text{C}$  using a cell hardware manufactured by Fuel Cell Technology Inc. The anode and cathode were fed with  $\text{H}_2$  and  $\text{O}_2$  respectively, at constant flow rates of  $0.5 \text{ slpm}$  at 100% relative humidity and  $150 \text{ kPa}$  absolute backpressure for both electrodes. EIS measurements were performed under galvanostatic control of the cell current and recorded using an integrated proprietary multi-channel impedance module. The selected frequency range for the EIS experiments was  $0.05 \text{ Hz}$  to  $10 \text{ kHz}$  and the amplitude of sinusoidal current signal corresponded to a cell voltage perturbation of  $10 \text{ mV}$  or lower to ensure that the measured impedance response satisfies linearity condition. The cell voltage was monitored during 3–5 min after applying current to ensure that the cell reached steady

state before EIS measurements. The accuracy of EIS measurements was about 1%.

### Model

The impedance model utilized in this work is based on the transient macro-homogeneous model for the cathode-side performance.<sup>44,45</sup> The performance model includes oxygen transport equations in the cathode channel, gas-diffusion layer and in the CCL. Oxygen transport along the channel and through the GDL and CCL depth are linked in a  $1\text{d} + 1\text{d}$  manner. In the CCL, oxygen transport is coupled to the proton charge conservation equation by Tafel rate of the ORR. Boundary and interface conditions express continuity of the oxygen concentration and flux at the channel/GDL and GDL/CCL interfaces. Oxygen flux at the membrane surface and proton current at the CCL/GDL interface are assumed to be zero.

Linearization and Fourier-transform of the performance equations lead to the system of linear equations for the perturbation amplitudes of oxygen concentration and local overpotential.<sup>44,45</sup> The cell is separated into  $N = 8$  virtual segments; numerical solution of the linear system results in the local model impedance  $Z_{\text{seg}}$  of each segment. The total cell impedance  $Z_{\text{tot}}$  is calculated from

$$\frac{1}{Z_{\text{tot}}} = \frac{1}{N} \sum_{n=1}^N \frac{1}{Z_{\text{seg},n}}, \text{ where } Z_{\text{seg},n} = \left( \frac{1}{Z_{\text{mod},n}} + i\omega C_{\text{ext}} \right)^{-1} + R_H \quad [1]$$

Here,  $Z_{\text{seg},n}$  is the segment impedance,  $Z_{\text{mod},n}$  is the model impedance,  $R_{\text{HFR}}$  is the high-frequency (membrane) resistance.

Equation 1 is equivalent to the circuit depicted in Fig. 1. The external capacitance  $C_{\text{ext}}$  (Fig. 1) models capacitance of a double layer (DL) at the catalyst/water interface. This interface has no direct connection to Nafion film and hence it does not participate in the ORR. However, water in the cell is a weak electrolyte and the DL at the catalyst/water interface contributes to the cell impedance. Introduction of  $C_{\text{ext}}$  improves the fitting quality of standard Pt/C-based PEMFCs spectra in the HF region<sup>43</sup> (see also discussion below).

The impedance model includes the following parameters: the ORR Tafel slope  $b$ , the CCL proton conductivity  $\sigma_p$ , the double layer capacitance  $C_{\text{dl}}$ , and the CCL and GDL oxygen diffusivities  $D_{\text{ox}}$  and  $D_p$ , respectively. Two more parameters are shown in Fig. 1: these are  $R_{\text{HFR}}$  and  $C_{\text{ext}}$ ; thus, in total seven parameters have been fitted to experimental points. The merit function to be minimized is

$$\sum_i \{ (\text{Re}(Z_{\text{tot},i}) - \text{Re}(Z_{\text{exp},i}))^2 + (\text{Im}(Z_{\text{tot},i}) - \text{Im}(Z_{\text{exp},i}))^2 \} \quad [2]$$

where  $Z_{\text{exp}}$  is the experimental impedance and the summation is performed over all frequency points.

Fitting has been performed using a custom Python code. The complex linear boundary-value problem for the perturbation amplitudes has been converted to equivalent real system for the real and imaginary parts of unknown functions. This system has been solved using the boundary value solver *solve\_bvp* from the SciPy library. Fitting itself has been done using the nonlinear least-squares procedure *least\_squares* from SciPy. The code has been parallelized using a standard message passing interface (MPI) library to take advantage of the multi-core architecture of modern processors. Fitting of a single spectrum on a 32-core cluster of 1.4-GHz ARM processors takes about one hour.

### Results and Discussion

Figures 2 and S1 (supplementary material is available online at [stacks.iop.org/JES/167/084501/mmedia](https://stacks.iop.org/JES/167/084501/mmedia)) show experimental and fitted Nyquist spectra for the cell with  $125\text{-}\mu\text{m}$  thick membrane. The frequency dependency of the imaginary parts of the impedance is presented in Figs. 3 and S2 for the same conditions. At the highest frequencies between  $5 \text{ kHz}$  and  $2 \text{ kHz}$ , the Nyquist plot in Fig. 2b,

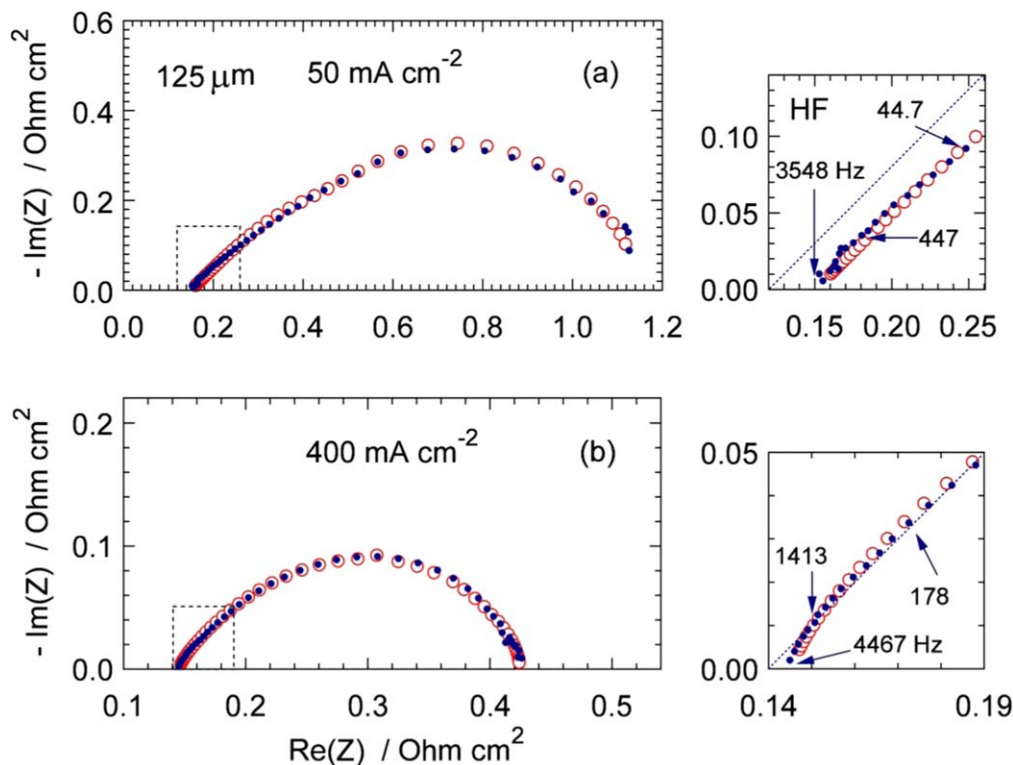


**Figure 2.** Experimental (solid points) and fitted model (open circles) Nyquist plots of the Fe–N–C–based PEM fuel cell with the Nafion membrane of a thickness 125  $\mu\text{m}$ . The experimental and model points are shown for the same set of frequencies. Right panels depict the high-frequency part of the spectra. A dotted, straight line of 45° is shown as a guide for the eye.

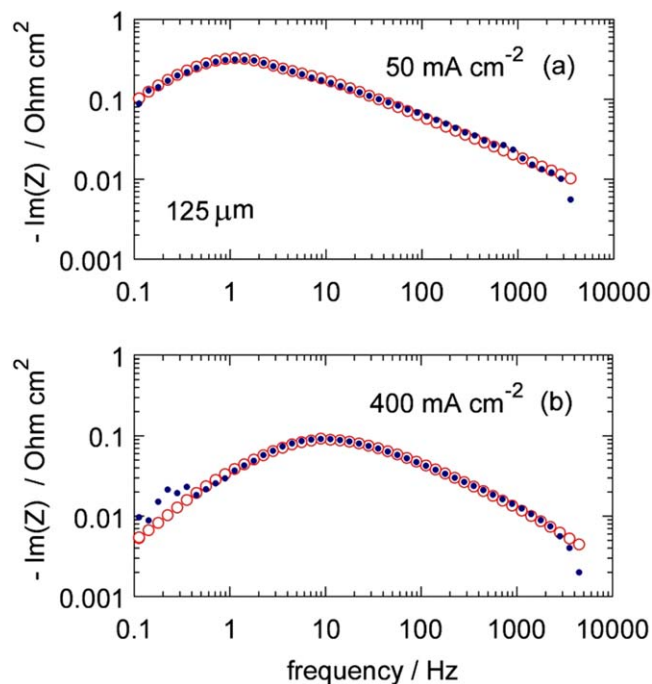


**Figure 3.** Experimental (solid points) and fitted model (open circles) frequency dependencies of imaginary part of impedance.

(right panel) exhibits a quite large curvature, an arc. We attribute this arc to impedance of the external capacitance  $C_{ext}$ ; however, the effect of  $C_{ext}$  is localized at the frequencies above 2 kHz.

At 400  $\text{mA cm}^{-2}$ , the HF arc is followed by a straight line with the slope of 45° (Fig. 2b, right panel). This straight line exhibits impedance due to proton transport in the cell.<sup>12,40</sup> At 50  $\text{mA cm}^{-2}$ ,

the slope of the straight line is somewhat lower due to superposition of proton transport and faradaic impedance. The characteristic angular frequency of proton transport is

$$\omega_p \simeq \frac{3\sigma_p}{C_{dl}l_t^2} \quad [3]$$

where  $C_{dl}$  is the catalyst/Nafion double layer capacitance and  $l_t$  is the CCL thickness. With the data from Table I, we get  $\omega_p \simeq 7 \text{ s}^{-1}$ . The characteristic frequency of faradaic (charge-transfer) processes is proportional to the cell current density:

$$\omega_{ct} \simeq \frac{j_0}{bC_{dl}l_t} \quad [4]$$

where  $b$  is the ORR Tafel slope per exponential basis. With the data from Table I,  $b = 0.03 \text{ V}$  and  $j_0 = 0.05 \text{ A cm}^{-2}$ , we obtain  $\omega_{ct} \simeq 6 \text{ s}^{-1}$ , i.e., the charge-transfer and proton transport impedances are overlapping. However, for the cell current of 400  $\text{mA cm}^{-2}$ , we find  $\omega_{ct} \simeq 30 \text{ s}^{-1}$ , i.e., at high cell currents, the proton transport and faradaic processes are well separated on the frequency scale. As a consequence, the straight line in Fig. 2b (right panel) has a slope of 45°, while in Fig. 2a (right panel) the slope of the spectrum is lower due to faradaic impedance. Note that the frequency dependencies of the proton transport and charge-transfer processes are quite different,<sup>29</sup> and the model is able to separate them at all the currents.

The model does not fit well the imaginary part of impedance at the highest frequencies between 3 and 5 kHz (Figs. 3a, 3b). At high cell current, the model does not describe the irregular behavior of  $\text{Im}(Z_{tot})$  at the lowest frequencies, between 0.1 and 0.3 Hz (Fig. 3b). This behavior is seemingly due to transport of liquid water in the GDL and channels.<sup>48</sup> In the frequency range from 0.3 Hz to 3 kHz, i.e., over four decades, the model points are very close to the experimental data (Fig. 3). The same trends demonstrate fitted



**Table I. Geometrical, operating and transport parameters of the cathodes. Parameters marked with asterisk \* are taken for the estimates only; the exact values resulted from fitting are shown in Fig. 4.**

Catalyst loading, $\text{mg cm}^{-2}$	6.0
Catalyst layer thickness $l_c$ , $\mu\text{m}$	170
Membrane thickness $l_m$ , $\mu\text{m}$	125/175
Gas diffusion layer thickness $l_g$ , $\mu\text{m}$	235
Relative humidity of pure oxygen	100%
Cathode absolute pressure, kPa	150
Cell temperature, K	273 + 80
Oxygen flow stoichiometry	>9.5
CCL heat transport coefficient $\lambda_r$ , $\text{W m}^{-1}\text{K}^{-1}$	0.27 <sup>46</sup>
ORR entropy change, $\text{J mol}^{-1}\text{K}^{-1}$	326.36 <sup>47</sup>
CCL proton conductivity* $\sigma_p$ , $\text{S cm}^{-1}$	0.01
CCL double layer capacitance* $C_{dl}$ , $\text{F cm}^{-2}$	30
ORR Tafel slope* $b$ , $\text{mV/exp}$	50
ORR overpotential* $\eta_0$ at $400 \text{ mA cm}^{-2}$ , V	0.5

spectra of the MEA with the membrane thickness of  $175 \mu\text{m}$  (Figs. S3 and S4).

The cell parameters derived from fitting are shown in Fig. 4. The cell with membrane thickness of  $175 \mu\text{m}$  exhibits extremely high ORR Tafel slope at the cell currents above  $400 \text{ mA cm}^{-2}$ ; the respective points are hardly reliable and not shown in Figs. 4a, 4c. However, below  $400 \text{ mA cm}^{-2}$ , the ORR Tafel slopes from the two cells are very close to each other, increasing almost linearly with the current density (Fig. 4a).

Since pure oxygen at the high stoichiometry (>9.5) has been used, the impedance due to oxygen transport in the GDL and channel is negligibly small and the model was not able to capture it. Of large interest are the plots of CCL proton conductivity  $\sigma_p$  and double layer capacitance  $C_{dl}$  (Figs. 4b, 4c). In  $125 \mu\text{m}$ -membrane cell, at the cell current of  $100 \text{ mA cm}^{-2}$ ,  $\sigma_p$  rapidly decreases from the low-current value of  $15\text{--}18 \text{ mS cm}^{-1}$  down to  $4\text{--}10 \text{ mS cm}^{-1}$  at higher currents (Fig. 4b). In the  $175 \mu\text{m}$ -membrane cell,  $\sigma_p$  varies in the range of 4 to  $13 \text{ mS cm}^{-1}$  showing no distinct correlation with  $j_0$  (Fig. 4b). However, the same rapid decay at  $100 \text{ mA cm}^{-2}$  exhibit the proton conductivity curves for the cells with membrane thicknesses of 15 and  $25 \mu\text{m}$  (to be published elsewhere).

The variations of  $\sigma_p$  with the cell current are accompanied by the variations of double layer capacitance (Fig. 4c). At high currents,  $C_{dl}$  in both the cells varies in the range of  $30$  to  $60 \text{ F cm}^{-2}$ , while at low currents, the  $125\text{-}\mu\text{m}$  cell exhibits low values of  $C_{dl} \approx 10\text{--}15 \text{ F cm}^{-2}$ . Note that the CCL proton conductivity and double layer capacitance change with the cell current exactly in counter-phase: large  $\sigma_p$  corresponds to low  $C_{dl}$  and vice versa (Figs. 4b, 4c). The impedance measurements have been performed using the pristine MEAs at the current densities in the ascending order, starting from  $25 \text{ mA cm}^{-2}$ . Rapid decay of proton conductivity in the  $125\text{-}\mu\text{m}$  cell at the cell current of  $100 \text{ mA cm}^{-2}$  (Fig. 4b) could be due to dissolution of Fe-N centers and poisoning of Nafion by  $\text{Fe}^{3+}$  ions. The equilibrium potential for  $\text{Fe}^{2+}/\text{Fe}^{3+}$  formation is  $0.77 \text{ V}$  vs RHE.<sup>49</sup> Polarization curve of the  $125 \mu\text{m}$ -membrane cell shows that the cell potential drops below this value at the current density around  $100 \text{ mA cm}^{-2}$  (Fig. 5), which is a strong argument in favor of this mechanism. Strong affinity of  $\text{Fe}^{3+}$  cations to fixed  $\text{SO}_3^-$  groups in the Nafion film may lead to formation of bind complexes  $3\text{SO}_3^-/\text{Fe}^{3+}$  (Refs. 50, 51). Close to the surface of electron-conducting phase,  $3\text{SO}_3^-/\text{Fe}^{3+}$  dipoles could form a kind of Stern double layer (DL), which would contribute to the total DL capacitance. Another reason for rapid conductivity decay in Fig. 4b (solid curve) could be removal of liquid water from the CCL by pressure gradient (see discussion below). This conjecture agrees with the fast growth of CCL oxygen diffusivity at low currents (Fig. 4d). The last option is destruction of Nafion side chains due to attack of

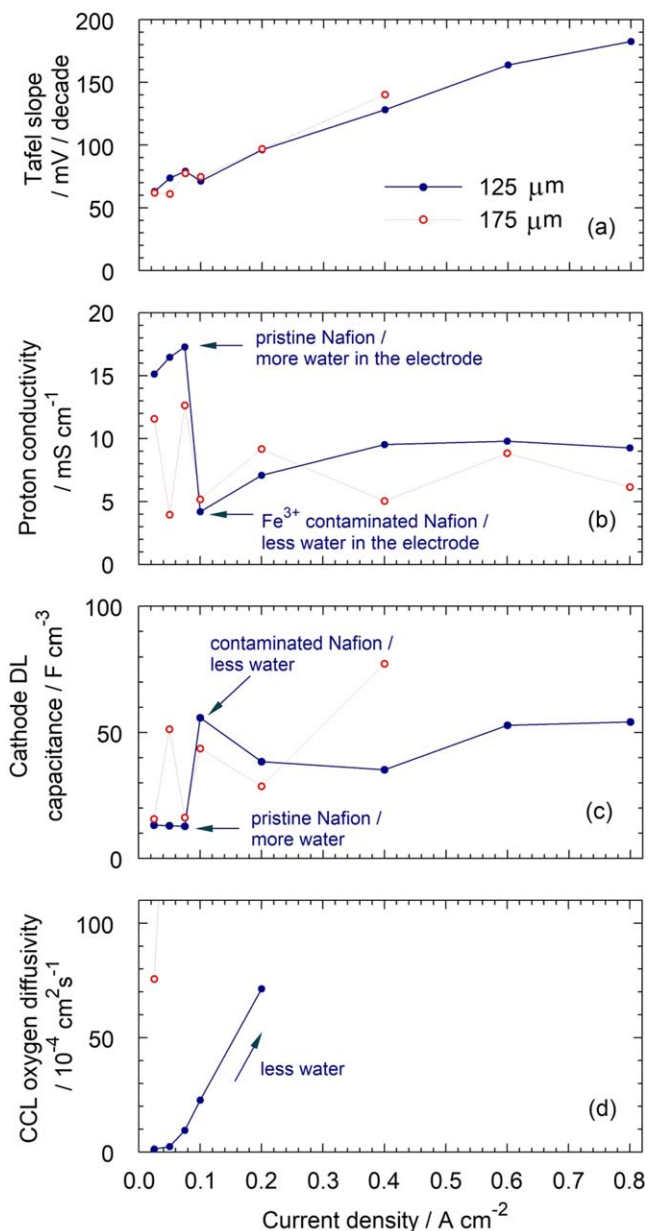


**Figure 4.** Fitting parameters for the cells with membrane thickness of  $125$  and  $175 \mu\text{m}$ . See text for discussion.

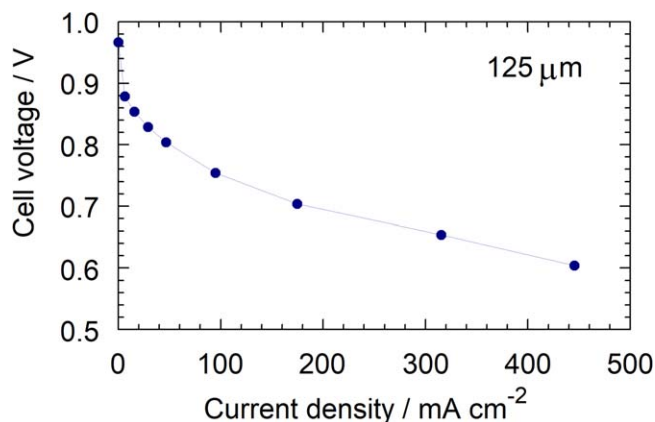


**Figure 5.** Polarization curve of the cell with  $125 \mu\text{m}$ -membrane.

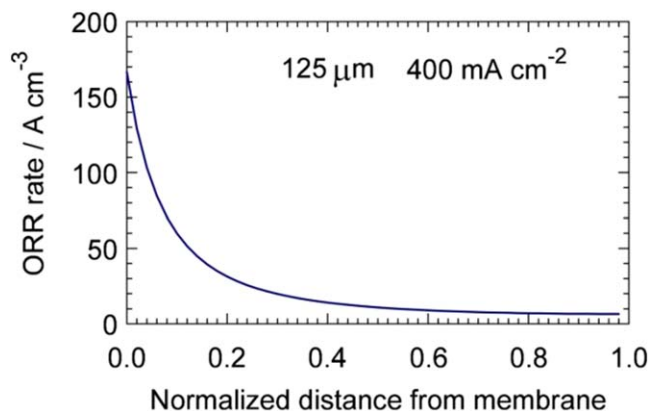


**Figure 6.** ORR rate through the catalyst layer depth for the cell current density of 400 mA cm<sup>-2</sup>.

radicals produced in Fenton's reaction of Fe<sup>3+</sup>/Fe<sup>2+</sup> ions with peroxide.<sup>52</sup> This mechanism has been investigated with regard to bulk Nafion degradation<sup>52,53</sup>; however, kinetic studies show that the proton conductivity degradation rate associated with Fenton's reactions is rather slow, typically it shows up on a scale of tens of hours.<sup>52</sup> Furthermore, this mechanism does not explain the observed simultaneous growth of double layer capacitance (Figs. 4b, 4c).

In both the cells, the external capacitance  $C_{ext}$  varies from 10<sup>-4</sup> F cm<sup>-3</sup> at low cell currents to about 0.3 F cm<sup>-3</sup> at high currents. In Pt/C-based PEMFCs,  $C_{ext}$  is about 10 F cm<sup>-3</sup>, and it strongly affects the HF part of the spectra.<sup>43</sup> Here, the upper value of  $C_{ext}$  is much less than the catalyst/Nafion double layer capacitance (10 to 50 F cm<sup>-3</sup>, Fig. 4c). Irregular behavior of  $C_{ext}$  could be due to uncontrollable amount of impurities in the cathode. Due to small value,  $C_{ext}$  practically does not change the shape of model spectra at the frequencies above 2 kHz.

The CCL oxygen diffusivity  $D_{ox}$  exhibits explosive growth with the cell current, rapidly increasing to extremely high values (Fig. 4d). At high cell currents, the contribution of oxygen transport impedance to  $Z_{tot}$  becomes negligibly small and the model was not able to correctly capture it. Rapid growth of  $D_{ox}$  with the cell current can be explained by formation of temperature and pressure gradients "pushing" liquid water out of the CCL. The temperature and pressure gradients could arise due to non-uniform distribution of the ORR rate through the CCL depth.

Indeed, the proton conductivity on the order of 10 mS cm<sup>-1</sup> is too low for the thick 170-μm cathodes used in both the cells. The characteristic current density  $j_p$  for proton transport in the CCL is<sup>37</sup>

$$j_p = \frac{\sigma_p b}{l_t} \quad [5]$$

With the parameters from Table I, we get  $j_p \simeq 30$  mA cm<sup>-2</sup>. This means that already at the current density of 50 mA cm<sup>-2</sup>, the ORR rate peaks at the membrane surface, while the remaining part of the catalyst layer is practically inactive. At the high CCL oxygen diffusivity, the distribution of ORR rate  $Q_{ORR}$  (A cm<sup>-2</sup>) in the CCL at high currents is described by<sup>53</sup>

$$Q_{ORR} \equiv -\frac{\partial j}{\partial x} = \frac{\sigma_p b}{2l_t^2} \beta^2 \left( 1 + \tan^2 \left( \frac{\beta}{2} (1 - \tilde{x}) \right) \right) \quad [6]$$

where  $\tilde{x} = x/l_t$  is the normalized distance through the CCL depth, and  $\beta$  is the solution to equation

$$\beta \tan \left( \frac{\beta}{2} \right) = \frac{j_0 l_t}{\sigma_p b} \quad [7]$$

Figure 6 shows the shape of  $Q_{ORR}$  for the parameters in Table I and the cell current density of 400 mA cm<sup>-2</sup>. Due to poor proton conductivity, the ORR rate is strongly non-uniform along  $\tilde{x}$ : it peaks at the membrane interface, where the "expenses" for proton transport are lower. This regime of CCL operation leads to doubling of apparent Tafel slope, which is detrimental for the cell performance.<sup>37</sup> Note that the ORR Tafel slope in Fig. 4a is the effective kinetic value, which does not include proton transport effects. Doubling of apparent Tafel slope means that at large currents, the slope of polarization curve would be twice larger than the slope depicted in Fig. 4a.

Two orders of magnitude difference between the ORR rate at the membrane surface and at the CCL/GDL interface ( $\tilde{x} = 1$ ) in Fig. 6 means that the reversible and irreversible reaction heat is released at the membrane surface. This could lead to quite substantial temperature gradient  $\Delta T$  over the catalyst layer thickness. In the regime shown in Fig. 6, the temperature drop  $\Delta T \equiv T_0 - T_1$  over the electrode thickness is given by<sup>54</sup>

$$\Delta T = \left( \frac{T_1 \Delta S}{4F} + \eta_0 + b \right) \frac{j_0 l_t}{\lambda_T} \quad [8]$$

Here,  $T_0$ ,  $T_1$  are the temperatures at the membrane surface and CCL/GDL interface, respectively,  $\Delta S$  is the entropy change in the ORR,  $\eta_0$  is the overpotential at the membrane surface. Eq. (8) contains the CCL thermal conductivity  $\lambda_T$ , which is not known for the Fe-N-C systems discussed. However, to a first approximation  $\lambda_T$  can be taken equal to the thermal conductivity of a standard Pt/C-based cathode. With the data from Table I,  $T_1 = 273 + 80$  K and  $j_0 = 0.4 \cdot 10^4$  A m<sup>-2</sup>, we get  $\Delta T \simeq 2.1$  K. This is quite a significant gradient, which may lead to pressure-induced flow of liquid water in the CCL. As gaseous oxygen transport is nearly three orders of magnitude faster than the transport in water, cleaning of CCL from liquid water would dramatically increase the effective oxygen diffusion coefficient of the porous media (Fig. 4d).

Finally, it is worth noting that the goal of model-based impedance spectroscopy is to extract physical transport parameters from the spectra. Verification of the mechanisms discussed above would require more EIS studies in different operating conditions as well as atomistic and computational fluid dynamics modeling.

## Conclusions

A model-based analysis of experimental impedance spectra of the cells with Fe-N-C-based cathodes has been performed. The spectra of two oxygen-fed cells differing by the membrane thickness only have been measured in the range of cell currents from 25 to 800 mA cm<sup>-2</sup>. A numerical impedance model which includes proton and oxygen transport in the catalyst layer has been fitted to experimental spectra.

- The ORR Tafel slope exhibits almost linear growth with the cell current density, from 50 mV/decade at low cell current up to 180 mV/decade at 800 mA cm<sup>-2</sup>.

- The CCL proton conductivity  $\sigma_p$  in the 125-μm cell exhibits rapid decay at the cell current of 100 mA cm<sup>-2</sup>; in the 175-μm cell and in the 125-μm cell at higher currents it varies in the range of 3 to 10 mS cm<sup>-1</sup>, without any clear dependence on the cell current. However,  $\sigma_p$  exhibits strong correlation with the double layer capacitance  $C_{dl}$ : low  $\sigma_p$  corresponds to large  $C_{dl}$  and vice versa. Possible mechanism of  $\sigma_p$  decay is dissolution of Fe-N-C centers with formation of Fe<sup>3+</sup> cations. Due to strong affinity to SO<sub>3</sub><sup>-</sup> groups, Fe<sup>3+</sup> ions lower the Nafion proton conductivity. In addition, 3SO<sub>3</sub><sup>-</sup>/Fe<sup>3+</sup> dipoles located close to the electron-conducting phase could increase the DL capacitance. Another reason for concerted counterphase variation of  $\sigma_p$  and  $C_{dl}$  could be liquid water removal from the catalyst layer by pressure gradient. The third mechanism of conductivity loss is Nafion film attack by radicals produced in Fenton's reaction of iron ions with peroxide; however, this

mechanism does not explain the observed simultaneous growth of double layer capacitance.

• Due to relatively low proton conductivity and large CCL thickness, the ORR rate is strongly non-uniform through the CCL depth. Estimates show that this non-uniformity leads to  $\approx 2$  K overheat of the catalyst layer at the membrane surface. The overheat could induce pressure gradient, pushing liquid water out of the CCL and clearing void pores for gaseous transport of oxygen. This mechanism might explain explosive growth of the CCL oxygen diffusivity with the cell current density derived from spectra fitting.

### Acknowledgments

TR gratefully acknowledges funding from US Office of Naval Research (N00014-18-1-2127, N00014-19-1-2159). MO, BZ, AS and TR gratefully acknowledge financial support from US DOE EERE (DE-EE0008419 “Active and Durable PGM-free Cathodic Electrocatalysts for Fuel Cell Application”). The authors are thankful to the Hawaiian Electric Company for ongoing support of the Hawaii Sustainable Energy Research Facility.

### ORCID

Andrei Kulikovskiy  <https://orcid.org/0000-0003-1319-576X>

### References

1. S. T. Thompson and D. Papageorgopoulos, “Platinum group metal-free catalysts boost cost competitiveness of fuel cell vehicles.” *Nature Cat.*, **2**, 558 (2019).
2. S. T. Thompson, A. R. Wilson, P. Zelenay, D. J. Myers, K. L. More, K. C. Neyerlin, and D. Papageorgopoulos, “ElectroCat: DOE’s approach to PGM-free catalyst and electrode R&D.” *Solid State Ionics*, **319**, 68 (2018).
3. U. Martinez, S. K. Babu, E. F. Holby, and P. Zelenay, “Durability challenges and perspective in the development of PGM-free electrocatalysts for the oxygen reduction reaction.” *Current Opinion Electrochem.*, **9**, 224 (2018).
4. D. A. Cullen, K. L. More, K. C. Neyerlin, H. T. Chung, P. Zelenay, and D. J. Myers, “Resolving active sites in atomically dispersed electrocatalysts for energy conversion applications.” *Microsc. Microanal.*, **25**, 2066 (2019).
5. K. Artyushkova, A. Serov, S. Rojas-Carbonell, and P. Atanassov, “Chemistry of active sites for oxygen reduction reaction in transition metal-nitrogen-carbon electrocatalysts.” *J. Phys. Chem. C*, **46**, 25917 (2015).
6. U. Martinez, E. F. Holby, S. K. Babu, K. Artyushkova, L. Lin, S. Choudhury, G. M. Purdy, and P. Zelenay, “Experimental and theoretical trends of PGM-free electrocatalysts for the oxygen reduction reaction with different transition metals.” *J. Electrochem. Soc.*, **166**, F3136 (2019).
7. L. Osmieri, “Transition metal–nitrogen–carbon (m–n–c) catalysts for oxygen reduction reaction. Insights on synthesis and performance in polymer electrolyte fuel cells.” *ChemEngineering*, **3**, 16 (2019).
8. D. Macdonald, “Reflections on the history of electrochemical impedance spectroscopy.” *Electrochim. Acta*, **51**, 1376 (2006).
9. M. E. Orazem and B. Tribollet, *Electrochemical Impedance Spectroscopy* (Wiley, New York) 2nd ed. (2017).
10. A. Lasia, *Electrochemical Impedance Spectroscopy and its Applications* (Springer, New York) (2014).
11. T. E. Springer, T. A. Zawodzinski, M. S. Wilson, and S. Gottesfeld, “Characterization of polymer electrolyte fuel cells using AC impedance spectroscopy.” *J. Electrochem. Soc.*, **143**, 587 (1996).
12. M. Eikerling and A. A. Kornyshev, “Electrochemical impedance of the cathode catalyst layer in polymer electrolyte fuel cells.” *J. Electroanal. Chem.*, **475**, 107 (1999).
13. Y. Bultel, L. Genies, O. Antoine, P. Ozil, and R. Durand, “Modeling impedance diagrams of active layers in gas diffusion electrodes: diffusion, ohmic drop effects and multistep reactions.” *J. Electroanal. Chem.*, **527**, 143 (2002).
14. F. Jaouen and G. Lindbergh, “Transient techniques for investigating mass-transport limitations in gas diffusion electrode.” *J. Electrochem. Soc.*, **150**, A1699 (2003).
15. Q. Guo, M. Cayetano, Y. Tsou, E. S. De Castro, and R. E. White, “Study of ionic conductivity profiles of the air cathode of a PEMFC by AC impedance spectroscopy.” *J. Electrochem. Soc.*, **150**, A1440 (2003).
16. Q. Guo and R. E. White, “A steady-state impedance model for a PEMFC cathode.” *J. Electrochem. Soc.*, **151**, E133 (2004).
17. Y. Bultel, K. Wietzel, F. Jaouen, P. Ozil, and G. Lindbergh, “Investigation of mass transport in gas diffusion layer at the air cathode of a PEMFC.” *Electrochim. Acta*, **51**, 474 (2005).
18. D. Gerteisen, A. Hakenjos, and J. O. Schumacher, “AC impedance modelling study on porous electrodes of proton exchange membrane fuel cells using an agglomerate model.” *J. Power Sources*, **173**, 346 (2007).
19. A. A. Franco, P. Schott, C. Jallut, and B. Maschke, “A multi-scale dynamic mechanistic model for the transient analysis of PEMFCs.” *Fuel Cells*, **7**, 99 (2007).
20. M. Cimenti, D. Bessarabov, M. Tam, and J. Stumper, “Investigation of proton transport in the catalyst layer of PEM fuel cells by electrochemical impedance spectroscopy.” *ECS Trans.*, **28**, 147 (2010).
21. I. A. Schneider, M. H. Bayer, and S. von Dahlen, “Locally resolved electrochemical impedance spectroscopy in channel and land areas of a differential polymer electrolyte fuel cell.” *J. Electrochem. Soc.*, **158**, B343 (2011).
22. J. Mainka, G. Maranzana, A. Thomas, J. Dillet, S. Didierjean, and O. Lottin, “One-dimensional model of oxygen transport impedance accounting for convection perpendicular to the electrode.” *Fuel Cells*, **12**, 848 (2012).
23. J. R. Vang, S. J. Andreasen, and S. K. Kaer, “A transient fuel cell model to simulate HTPM fuel cell impedance spectra.” *J. Fuel Cell Sci. Technol.*, **9**, 021005 (2012).
24. A. A. Kulikovskiy, “Exact low-current analytical solution for impedance of the cathode catalyst layer in a PEM fuel cell.” *Electrochim. Acta*, **147**, 773 (2014).
25. A. A. Kulikovskiy, “One-dimensional impedance of the cathode side of a PEM fuel cell: Exact analytical solution.” *J. Electrochem. Soc.*, **162**, F217 (2015).
26. T. Reshetenko and A. Kulikovskiy, “PEM fuel cell characterization by means of the physical model for impedance spectra.” *J. Electrochem. Soc.*, **162**, F627 (2015).
27. A. Baricci and A. Casalegno, “A simple analytical approach to simulate the electrochemical impedance response of flooded agglomerates in polymer fuel cells.” *Electrochim. Acta*, **157**, 324 (2015).
28. D. Gerteisen, “Impact of inhomogeneous catalyst layer properties on impedance spectra of polymer electrolyte membrane fuel cells.” *J. Electrochem. Soc.*, **162**, F1431 (2015).
29. A. A. Kulikovskiy, “A simple physics-based equation for low-current impedance of a PEM fuel cell cathode.” *Electrochim. Acta*, **196**, 231 (2016).
30. T. Reshetenko and A. Kulikovskiy, “Impedance spectroscopy study of the PEM fuel cell cathode with nonuniform nafion loading.” *J. Electrochem. Soc.*, **164**, E3016 (2017).
31. T. Reshetenko and A. Kulikovskiy, “Impedance spectroscopy characterization of oxygen transport in low- and high- $p_t$  loaded PEM fuel cells.” *J. Electrochem. Soc.*, **164**, F1633 (2017).
32. A. M. Niroumand, W. Merida, M. Eikerling, and M. Saif, “Pressure-voltage oscillations as a diagnostic tool for PEFC cathodes.” *Electrochem. Comm.*, **12**, 122 (2010).
33. E. Engebreetsen, T. J. Mason, P. R. Shearing, G. Hinds, and D. J. L. Brett, “Electrochemical pressure impedance spectroscopy applied to the study of polymer electrolyte fuel cells.” *Electrochem. Comm.*, **75**, 60 (2017).
34. A. Sorrentino, T. Vidakovic-Koch, R. Hanke-Rauschenbach, and K. Sundmacher, “Concentration-alternating frequency response: a new method for studying polymer electrolyte membrane fuel cell dynamics.” *Electrochim. Acta*, **243**, 53 (2017).
35. A. Kulikovskiy, “A model for concentration impedance of a pem fuel cell.” *eTrans*, **2**, 100026 (2019).
36. M. Heinzmann, A. Weber, and E. Ivers-Tiffée, “Advanced impedance study of polymer electrolyte membrane single cells by means of distribution of relaxation times.” *J. Power Sources*, **402**, 24 (2018).
37. A. A. Kulikovskiy, “The regimes of catalyst layer operation in a fuel cell.” *Electrochim. Acta*, **55**, 6391 (2010).
38. D. Malevich, B. R. Jayasankar, E. Hallipi, J. G. Pharoah, B. A. Peppley, and K. Karan, “On the determination of PEM fuel cell catalyst layer resistance from impedance measurement in H<sub>2</sub>/N<sub>2</sub> cells.” *J. Electrochem. Soc.*, **159**, F888 (2012).
39. Y. Liu, C. Ji, W. Gu, J. Jorne, and H. A. Gasteiger, “Effects of catalyst carbon support on proton conduction and cathode performance in pem fuel cells.” *J. Electrochem. Soc.*, **158**, B614 (2011).
40. A. A. Kulikovskiy and M. Eikerling, “Analytical solutions for impedance of the cathode catalyst layer in PEM fuel cell: Layer parameters from impedance spectrum without fitting.” *J. Electroanal. Chem.*, **691**, 13 (2013).
41. R. Makharia, M. F. Mathias, and D. R. Baker, “Measurement of catalyst layer electrolyte resistance in PEMFCs using electrochemical impedance spectroscopy.” *J. Electrochem. Soc.*, **152**, A970 (2005).
42. T. Reshetenko, A. Serov, A. Kulikovskiy, and P. Atanassov, “Impedance spectroscopy characterization of PEM fuel cells with Fe–N–C–based cathodes.” *J. Electrochem. Soc.*, **166**, F653 (2019).
43. T. Reshetenko and A. Kulikovskiy, “On the origin of high frequency impedance feature in a PEM fuel cell.” *J. Electrochem. Soc.*, **166**, F1253 (2019).
44. A. A. Kulikovskiy, “A physical model for the catalyst layer impedance.” *J. Electroanal. Chem.*, **669**, 28 (2012).
45. A. Kulikovskiy and O. Shamardina, “A model for PEM fuel cell impedance: Oxygen flow in the channel triggers spatial and frequency oscillations of the local impedance.” *J. Electrochem. Soc.*, **162**, F1068 (2015).
46. M. Khandelwal and M. Mench, “Direct measurement of through-plane thermal conductivity and contact resistance in fuel cell materials.” *J. Power Sources*, **161**, 1106 (2006).
47. M. J. Lampinen and M. Fomino, “Analysis of free energy and entropy changes for half-cell reactions.” *J. Electrochem. Soc.*, **140**, 3537 (1993).
48. S. K. Roy and M. E. Orazem, “Analysis of flooding as a stochastic process in polymer electrolyte membrane (pem) fuel cells by impedance techniques.” *J. Power Sources*, **184**, 212 (2008).
49. Q. Jia et al., “Experimental observation of redox-induced Fe–N switching behavior as a determinant role for oxygen reduction activity.” *ACS Nano*, **9**, 12496 (2015).
50. K. Hongsirikarn Jr, J. G. Goodwin, S. Greenway, and S. Creager, “Effect of cations (Na<sup>+</sup>, Ca<sup>2+</sup>, Fe<sup>3+</sup>) on the conductivity of a Nafion membrane.” *J. Power Sources*, **195**, 7213 (2010).
51. A. Münchinger and K.-D. Kreuer, “Selective ion transport through hydrated cation and anion exchange membranes I. The effect of specific interactions.” *J. Membrane Sci.*, **592**, 117372 (2019).

52. T. Sugawara, N. Kawashima, and T. N. Murakami, "Kinetic study of Nafion degradation by Fenton reaction." *J. Power Sources*, **196**, 2615 (2011).
53. R. Coulon, W. G. Bessler, and A. A. Franco, "Modeling chemical degradation of a polymer electrolyte membrane and its impact on fuel cell performance." *ECS Trans.*, **25**, 259 (2010).
54. A. A. Kulikovsky and J. McIntyre, "Heat flux from the catalyst layer of a fuel cell." *Electrochimica Acta*, **56**, 9179 (2011).